Irreversible growth model for virus capsid assembly

Stephen D. Hicks* and C. L. Henley†
Department of Physics, Cornell University, Ithaca, New York 14853, USA
(Received 23 March 2006; revised manuscript received 8 August 2006; published 25 September 2006)

We model the spontaneous assembly of a capsid (a virus' closed outer shell) from many copies of identical units, using entirely irreversible steps and only information local to the growing edge. Our model is formulated in terms of (i) an elastic Hamiltonian with stretching and bending stiffness and a spontaneous curvature, and (ii) a set of rate constants for the addition of new units or bonds. An ensemble of highly irregular capsids is generated, unlike the well-known icosahedrally symmetric viruses, but (we argue) plausible as a way to model the irregular capsids of retroviruses such as HIV. We found that (i) the probability of successful capsid completion decays exponentially with capsid size; (ii) capsid size depends strongly on spontaneous curvature and weakly on the ratio of the bending and stretching elastic stiffnesses of the shell; (iii) the degree of localization of Gaussian curvature (a measure of facetedness) depends heavily on the ratio of elastic stiffnesses.

DOI: 10.1103/PhysRevE.74.031912 PACS number(s): 87.15.Nn, 87.15.Aa, 61.50.Ah, 81.16.Dn

I. INTRODUCTION

In recent years the question of spontaneous assembly has arisen in many apparently disconnected fields, including nanofabrication [1,2], robotics and microelectronics [3,4], and particularly, biology [5,6]. While the assembly of many biological structures, such as actin filaments and chromatin, requires energy in the form of ATP hydrolysis [7–9], numerous other structures assemble spontaneously. In particular are lipid bilayers [10,11] and virus capsids [12,13], the subject of this paper.

A. Quasiequivalence

The capsid of a virus is the shell of proteins surrounding and protecting the viral genome (DNA and RNA). Capsids are observed in a wide variety of sizes, ranging into the thousands of proteins; most known capsids have icosahedral or cylindrical point-group symmetry [14,15]. A typical virus uses only one, or a few, kinds of protein in its capsid; consequently noted, typical capsids are necessarily built from copies of the same unit in positions that are *not* equivalent by any global symmetry [16]. However, Caspar and Klug [16] identified an elegant approximate symmetry, which they called *quasiequivalence*. The key idea is that locally, every bit of the capsid is a patch of triangular lattice; in an infinite triangular lattice, all the units *would* be symmetry equivalent. They argued that typical proteins could accommodate a variation of ±5° in bond angles [17], while maintaining the same microscropic bonding between proteins. This allows the representation of any capsid as a network of approximately equilateral triangles, with a constraint (due to the bond angle limitation) that the number of triangles around every vertex must always be either five or six. The points of local fivefold symmetry may be identified with the topological defects called *disclinations* (to be defined in Sec. II A), and any closed shell must contain exactly twelve of them. In an icosahedral capsid, the disclinations form the vertices of a large icosahedron, the edges of which have length $\sqrt{T}$ in lattice units, where the triangulation number $T=1,3,4,7,\ldots$ is one of a sequence of discrete allowed integers [16], so that there are $60T$ small triangles.

We emphasize that the rules of quasiequivalence do not force any global symmetry, nor do they fix the size of the completed capsid. Thus it is surprising that many viruses reliably assemble large symmetric capsids. The challenge to theory is to explain both the size and shape selection, or at least to explain why a closed shell is formed, when tubes or sheets would be equally consistent with the local bonding. It would not be surprising if models predict different capsids depending on parameters (which might experimentally correspond to pH, salt content, catalysts, protein concentrations, or mutations in the capsid protein). Such polymorphic behavior is very fruitful to study in quasiequivalent models: it effectively explores more of the various local geometries in which the proteins can bind and thus can allow more parameters to be determined, in principle. This paper develops a model of irreversible (nonequilibrium) assembly of quasiequivalent units, which produces a highly polymorphic ensemble of capsids, which we argue below may model the growth of retrovirus capsids.

It is worth mentioning that Tworock [18] has developed virus tiling theory, an extension to Caspar-Klug quasiequivalence, which uses rhombs and kites rather than triangles, and can therefore describe the anomalous viruses from *Papovaviridae*.

B. Recent models

The most successful recent capsid models consistent with quasiequivalence are *equilibrium* theories: a microscopically motivated phenomenological Hamiltonian is shown to be optimized by certain shapes, and it is assumed that this free-energy minimum is found during the actual assembly process. Thus Bruinsma *et al.* [13,19] modeled pentamers and hexamers as different-sized disks packed on a sphere, with an effective Hamiltonian favoring dense packing, a bending stiffness with spontaneous curvature, and a switching cost to

*Electronic address: sdh33@cornell.edu
†Electronic address: clh@ccmr.cornell.edu

make pentamers (rather than hexamers) of the proteins. When this switching cost is small, icosahedral viruses were selected over nonicosahedral shapes [19]. Additionally, they demonstrated polymorphism, similar to phenomena seen in cowpea chlorotic mottle virus (CCMV), by showing a phase transition between tubes, $T=3$, and $T=1$ capsids as the model parameters varied. Another family of models, introduced by Nelson [20], focuses on the external shape of large capsids, using continuum elastic theory: the shape evolves from practically spherical to sharply faceted as the size increases or the bending stiffness decreases.

Alternate theories to quasiequivalence have also been developed, still in terms of an equilibrium picture. Most notable is the "local rules" theory [21–23], which posits *several* "flavors" of unit, with *inequivalent* edges, and rules for the joining of these different kinds of edges so the units fit together like puzzle pieces and there is a single unique structure that obeys all the matching rules. It is generally necessary to assume that the same capsid protein molecule has different conformation species, each of which has entirely different specific binding. It appears implausible that so many different functions could be built into one molecule, or that evolution could have discovered this solution, if it is the only way to engineer a large capsid. We therefore prefer a theory without such matching rules.

Another class of theory focuses on the *process* of assembly, which one might expect is far from equilibrium. In particular, Zlotnick [24,25] has focused on the kinetics of capsid growth. Using a basic unit of $5T$ proteins, so that the complete capsid is a dodecahedron of 12 units, and a free energy based on the number of adhered edges, he considers the species of the most stable incomplete capsid of any size and constructs rate equations relating the concentrations of each species. This leads to the phenomenon of the kinetic trap: if the initial concentration of monomers is too large, they aggregate quickly into larger structures, slowing the later stages of growth since the required monomers are depleted.

Similar kinetic models have been extended using the virus tiling theory [18]. Keef *et al.* [26] extend Zlotnick's work and consider the effect of different association energies on the kinetics of *Papovaviridae* assembly.

So far we have limited our discussion to icosahedral viruses. While there is some polymorphism in icosahedral viruses—usually changing T numbers under different conditions—the capsids are still generally symmetric. Mature retroviral capsids, on the other hand, have been observed to be very irregular [27].

C. Retroviruses

Retroviruses, such as human immunodeficiency virus (HIV) and rous sarcoma virus (RSV), are RNA viruses which all contain a characteristic enzyme—reverse transcriptase—allowing the RNA to be transcribed into DNA for infection. Upon infection, the virus produces copies of several proteins—in particular, the structural polyprotein Gag. Many copies of Gag (approximately 1500 for RSV [28] or 5000 for HIV [29]) aggregate at the cell membrane before budding out of the cell as an immature virus particle. A maturation step then takes place in which a protease cleaves Gag into its constituent proteins: matrix (MA), capsid (CA), and nucleocapsid (NC). After cleavage, the MA remain bound to the lipid membrane and the NC remain bound to the RNA. A fraction of the CA then reassemble into the mature capsid [30]. In HIV, this fraction has been measured to be roughly 30% [29,31].

Ganser *et al.* [27] proposed a model to point out that the cones formed by mature HIV cores must have quantized angles and measured this on electron micrographs. Later studies have measured these angles and other data using more accurate tomography [32,33]. In addition to the irregular structure, polymorphism is also observed in the switching between tubes, cones, and spheres under different conditions [34]. RSV, on the other hand, has cores that are observed to be roughly spherical, but with a wide distribution in the degree of asphericity [35].

There is a significant variation in the size and shape of mature HIV capsids, but they are commonly cones. Following the quasiequivalence paradigm, these are described geometrically by locally triangular lattices like carbon fullerene cones [36,37]. There is no well-established explanation of the cone's shape or size. Briggs *et al.* [32] suggest that the small end of the cone forms first, possibly from a sort of template, and that the large end forms when the growing capsid runs into the membrane. Benjamin *et al.* [33] instead suggest that the large end is nucleated first. Nguyen *et al.* [38] developed an equilibrium theory combining the ideas of Refs. [13,20], adding fullerene cones [37] to consideration. Assuming a fixed size, they generate a family of configurations of maximum symmetry, and find a phase transition between cones, tubes, and spheres as a function of the elastic parameters. A weakness of their model, however, is that cones are stable in a relatively small portion of parameter space, and their appearance at all depends critically on the assumption of a fixed size, which is unphysical. In HIV maturation, only one-third of the CA proteins assemble into the mature conical capsid, leaving the rest in solution within the virus' lipid envelope [29,30]. Thus, we should expect the capsid size to vary freely. Later work by Nguyen *et al.* [39] suggests that conical capsids are not energy minima, but are instead selected by assembly constraints.

D. Outline

In the following pages we present our model of capsid assembly, discussing our choice of energy and transitions, which govern the growth of a capsid from a single unit to a complete closed shell, by alternately minimizing the energy and choosing a transition to a larger capsid.

We discuss common failure modes in this model and the choices of parameters in which they arise. In particular, we look at a mostly avoidable failure, which occurs at the end of growth in which a small hole cannot be completed, and a more problematic failure, which occurs in the middle stages of growth and involves narrow "fingers" of capsid.

We then consider a number of ways to measure growing and complete capsids, largely motivated by experimental measurements. We present three main results. First, capsid

size depends primarily on the spontaneous curvature, but also on the ratio of elastic constants. Second, growth failure is a roughly Poissonian process, and thus the probability of successful growth decreases exponentially with the expected size. Third, we discuss the application of our model to various measurements of the shape of capsids, with particular emphasis on the Gaussian curvature.

Finally, we summarize our results and discuss the advantages and disadvantages of our model, and possible future directions.

II. IRREVERSIBLE GROWTH MODEL

We now introduce a model to describe quasiequivalent capsid assembly in a far-from-equilibrium picture. Consider a single growing capsid and a number of units in solution. We picture the units slowly accreting onto the growing capsid until the finished product is formed.

Our choice is to represent this by adopting the simplest possible model that can represent a growing capsid and be simulated efficiently: this precludes representing each protein as a rigid body moving in space. Instead, a capsid (growing or completed) is represented by a triangular network (Sec. II A), with an elastic energy governing the bond lengths and angles (Sec. II B). We do not explicitly represent the units in solution, instead formulating a set of first-order rate equations for the addition of a unit to the capsid or for other discrete changes in the network geometry (Sec. II C).

Other physical or mathematical models have been abstracted to a similar degree [13,19,20], following a standard philosophy of statistical mechanics. Some capacity to adapt the model to (say) a specific virus species is lost, but the simplicity makes it conceivable to grasp the physical meaning of each parameter, and feasible to explore all dimensions of the parameter space by simulations. Typically, only particular combinations of the microscopic parameters matter, and a properly formulated toy model adopts those combinations. It can happen that fairly different microscopic systems may, through such elimination of unimportant parameters, all map to the same simple model; in that case, the model offers a possibility of unifying the description of all these systems.

A. Configuration degrees of freedom

Our formulation depends on *two* complementary kinds of degree of freedom, a discrete kind we call "topological" and a continuous kind called "positional." The former consists of a bond network built from triangles, with vertices either connected by a bond or not; the latter consists of the actual coordinates of the vertices in space. Since prior work emphasized equilibrium, we took the opposite limit by allowing no change in any bond, once formed. One consequence is that our discrete "topological" variables are more fundamental than the positional ones: given a network of bonds, the angles and bond lengths will relax to a constrained minimum (or fluctuate thermally around it) as determined by a Hamiltonian, defined in Sec. II B. In our growth model, these positional variables feed back into the discrete ones by controlling the relative rates of alternative changes in the network as units are accreted. (In principle, one could envisage a further abstraction in which the positional variables are eliminated completely and the rates expressed directly in terms of the bond topology, but we did not attempt that.)

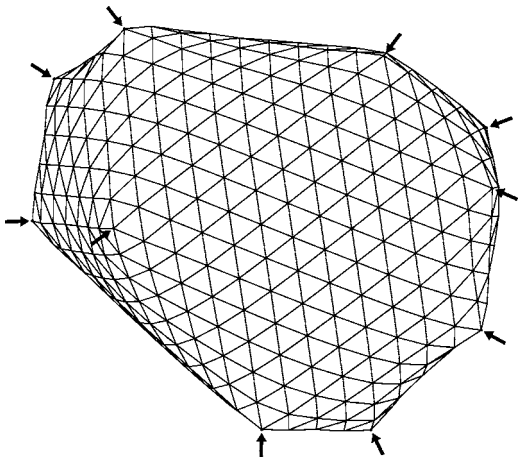

FIG. 1. Example of a closed final capsid resulting from our growth simulation, with $\ell_f=0.12r_0$, $\theta_0=16°$, $\Gamma_{I,J}=50$, and $\sigma=12.7°$. These parameters are explained in Secs. II B and II C. The disclinations are marked by arrows.

The models discussed above in Sec. I B all have essentially just a single type of degree of freedom—the first, the second, or something intermediate. Lidmar *et al.* [20] assume a predetermined graph topology, so only the vertices' positions are nontrivial. On the other hand, Endres *et al.* [40] discard position information and only consider the (discrete) connectivity. Finally, Bruinsma *et al.* [13] continuously vary the positions of the disks, and determine which disks neighbor one another secondarily.

It may be questioned why we have chosen triangles as the fundamental building blocks. In a model more faithful to a particular virus species, one would want to add the multimer, which is accreted in nature. Virus species assembling from dimers [41,42], trimers [43], and pentamers (hexamers) [44], have all been observed experimentally. HIV has so far formed only dimers in solution [45]. Several groups have done molecular dynamics simulations using solutions of monomers [21,46] and kinetic simulations with pentamers [24], dimers [47], or trimers [48]. Because of its simplicity, and the work done on tethered surfaces by Nelson and coworkers [20,49], we will focus on a trimer-based model for this initial work, an example of which can be seen in Fig. 1. It is at this point worth noting that the hexagonal lattice, which is dual to our triangular lattice, is in fact very similar to the molecular lattices formed from HIV CA [50].

Our use of triangle units is also influenced by the notion of "universality" in physics, whereby the functional form of elastic theory, or the critical exponents of a phase transition, are independent of the particular lattice used at the microscopic scale. In any of the alternative representations, one can still define a triangular, locally sixfold lattice with rare locally fivefold points in it. Much experience in statistical mechanics suggests that, at "coarse-grained" length scales (those large compared to the lattice spacing), the behavior stops depending on the details. However, two related caveats

must be expressed: (i) possibly a detail of the microscopic model forces a certain parameter of the coarse-grained model to be strictly zero, thereby changing the qualitative behavior ("universality class"); (ii) it may be that a parameter regime easy to achieve in one version of the model will require a complicated fine-tuning of parameters in an alternate version.

Caspar and Klug [16] noted that only pentamers and hexamers have small enough deformations to be allowed in quasiequivalence, and thus any quasiequivalent capsid must have exactly twelve pentamers. Quasiequivalence is based on a flat triangular lattice, so that a pentamer is a *disclination:* a topological defect of the triangular lattice. This means it can be characterized by effects at an arbitrary distance; namely, if we parallel transport a vector around a loop, that vector ends up rotated by $(\pi/3)N_{\text{disc}}$ from its starting orientation, where N_{disc} is the number of fivefold disclinations enclosed by the loop. (This is called a "disclination charge" by the analogy to how the electric charge enclosed by a surface is determined by an integral of the electric field over that surface, according to Gauss's law.) That there are exactly twelve disclinations can now be seen either by counting vertices, edges, and triangles under the constraint $V-E+F=2$, or more generally because the total disclination charge must sum to 4π [51].

Between the disclinations are patches of regular sixfold lattice with no topological freedom: thus, *the capsid is completely determined by the placement of the disclinations*. Since there may be hundreds of network vertices, and only twelve disclinations, this is in principle a simplification.

B. Hamiltonian

We represent the growing capsid as a number of approximately equilateral triangles connected along the edges. We then generalize the discretized Hamiltonian used by Lidmar *et al.* [20] to include spontaneous curvature θ_0 and steric terms.

$$\mathcal{H} = \mathcal{H}_{\text{stretch}} + \mathcal{H}_{\text{bend}} + \mathcal{H}_{\text{steric}}. \tag{1}$$

1. Elastic energy

The first two terms in Eq. (1) are elastic terms for bond stretching and bending;

$$\mathcal{H}_{\text{stretch}} = \frac{\sqrt{3}\tilde{Y}}{4}\sum_{\langle ij\rangle}(|\mathbf{r}_i - \mathbf{r}_j| - r_0)^2, \tag{2}$$

$$\mathcal{H}_{\text{bend}} = \frac{2\tilde{\kappa}}{\sqrt{3}}\sum_{\langle IJ\rangle}[1 - \cos(\theta_{IJ} - \theta_0)]. \tag{3}$$

Here, $\langle ij\rangle$ denotes pairs of nearest-neighbor vertices with positions $\mathbf{r}_i$, and $\langle IJ\rangle$ denotes pairs of nearest-neighbor triangles. The exterior dihedral angle

$$\theta_{IJ} = \cos^{-1}(\hat{\mathbf{n}}_I \cdot \hat{\mathbf{n}}_J), \tag{4}$$

where $\hat{\mathbf{n}}_I$ is the unit normal to triangle I.

Our discretized parameters $\tilde{Y}$ and $\tilde{\kappa}$ have the same dimensions as the two-dimensional Young's modulus Y and bending stiffness κ, respectively, which are emphasized in continuum approaches to predicting capsid shapes [20], and for a flat sheet in the linearized regime the parameters have the same values as well. If we parametrized our model by spring constants K_{stretch} and K_{bend} equal to the curvature of our radial and angular potentials at the bottoms of their respective wells, we would have $\tilde{Y} = \frac{2}{\sqrt{3}}K_{\text{stretch}}$ and $\tilde{\kappa} = \frac{\sqrt{3}}{2}K_{\text{bend}}$. In most cases (except in direct comparison with some experimental measurements), we are only concerned with the ratio of these elastic constants. This ratio provides a length scale, the *Foppl–von Kármán length*,

$$\ell_f^2 \equiv \kappa/Y. \tag{5}$$

From this point on, we will take units such that $r_0=1$, and therefore the parameter ℓ_f is effectively dimensionless.

Previous work made this same ratio dimensionless using the capsid *radius* R, rather than the triangle size r_0, and thus defined the Foppl–von Kármán number [20]

$$\gamma = YR^2/\kappa. \tag{6}$$

The capsid radius R is well defined in the case of a spherical capsid, but for nonspherical capsids, a definition of R is problematic; and in any case, ℓ_f controls many other properties, such as the exponential decay of strain and the Gaussian curvature with distance from a defect. Thus, we consider ℓ_f to be the more fundamental parameter and thus write $\gamma = (R/\ell_f)^2$. We note that a small ℓ_f corresponds to a large Young's modulus and therefore an *angular* (or faceted) regime. On the other hand, large ℓ_f entails a large bending stiffness and leads to a *smooth* regime [20]. Since our model is two-dimensional, we are able to specify an arbitrarily large ℓ_f. Physically, however, ℓ_f must be on the order of the capsid thickness or smaller.

2. Spontaneous curvature and steric repulsion

Microscopically, we expect that capsid proteins are more similar in shape to cones or pyramids, with the apex toward the inside, than to cylinders [52]. Therefore, if two proteins are in contact, the outer surface will be bent at a characteristic angle. This suggests that $\mathcal{H}_{\text{bend}}$ should favor some dihedral angle θ_0, appearing in Eq. (3). Additionally, it motivates our model of steric repulsion based on tetrahedra, explained below.

The preferred dihedral angle θ_0 is a key parameter since it is the main determinant of capsid size in our model, as was speculated to be the case in real capsids [16]. This corresponds to spontaneous curvature in a continuum model.

The final term $\mathcal{H}_{\text{steric}}$ in Eq. (1) is a steric potential, chosen to vanish for all physically realistic capsids. The steric potential proves difficult to incorporate into our cartoon model, for two reasons. Firstly, all the interunit interactions of properly bonded units should already be accounted for in the elastic term $\mathcal{H}_{\text{stretch}}+\mathcal{H}_{\text{bend}}$, so we demand that the steric force not make additional contributions to these forces. Secondly, the other terms in Eq. (1) relate units that are "topological neighbors," as defined by the bond network (the dis-

crete configuration). But two topologically distant parts of the capsid, may grow to be nearby in real space (the positional configuration), and must then be kept from intersecting. Thus, the steric term must apply equally to topologically distant segments of the capsid, or to adjacent units, e.g., two as yet unjoined triangles on the same vertex.

To implement a computationally tractable steric potential, we imagine each triangle to be the base of an inward-pointing tetrahedron, and add a repulsion between the apex of each tetrahedron and the vertices on the base of each other. This potential vanishes for physically realistic capsids. A more technical discussion may be found in Appendix B, and the steric Hamiltonian is defined in Eq. (B1).

3. Microscopic estimation of elastic energy

Interactions between capsid proteins have been simulated electrostatically [14] to determine binding energies for large multimers of capsid proteins, necessarily in different relative positions. Such simulations could be extended to determine the elastic constants for particular viruses with known protein structure.

Alternatively, we can perform a rough estimate of the elastic parameters by considering some experimental measurements. Vliegenthart and Gompper [53] performed extensive computational studies to relate experiments with atomic force microscope (AFM) indentation of capsids to a model very similar to ours. Thus, we can use these AFM studies to determine the appropriate magnitude of Y and κ. Ivanovska *et al.* [54] carried out mechanical structure measurements on the $T=3$ phage $\phi 29$ and found the bulk modulus $B \approx 1.4$ GPa and the thickness $t \approx 2.5$ nm. We obtain an estimate of the two-dimensional Young's modulus by $Y \sim Bt \approx 3.5$ N/m [38].

We could also estimate the elastic parameters from persistence length measurements. Maeda and Fujime [55] measured the tube-forming phage *fd* in suspension and determined the persistence length of the 9-nm-diameter tubes at 22 °C to be 3.9 μm. If we construct a tube out of our triangular units, the persistence length would be

$$\xi_p \approx \frac{R}{k_B T}\left(\kappa + \frac{8}{9} Y R^2\right), \tag{7}$$

where R is the radius of the tube. Thus, we can conclude $\kappa + (8/9) Y R^2 = Y[(8/9)R^2 + \ell_f^2] \approx 22$ eV, which puts an upper bound of 0.17 N/m on Y, in sharp contrast to the $\phi 29$ results above. Moreover, since *fd* is charged [56], the purely elastic contribution to the persistence length may be much smaller, making our estimate very conservative. If we previously knew either ℓ_f or one of Y or κ, we could use this measurement to determine the others.

To get an idea of the elastic parameters for HIV, we can produce model capsids by hand, which resemble HIV cores. In particular, we grew several capsids with about 500 triangles in a cone shape. Tuning the elastic parameters to roughly match the observed shape of HIV [33,53], we found $\gamma = (R/\ell_f)^2 \approx 550$ produces the correct amount of facetedness. This corresponds to $r_0/\ell_f = 6$. Using our results for capsid size as a function of ℓ_f and θ_0, presented in Sec. IV A, we can guess that such a capsid would require $\theta_0 \approx 20°$ to be grown by our model.

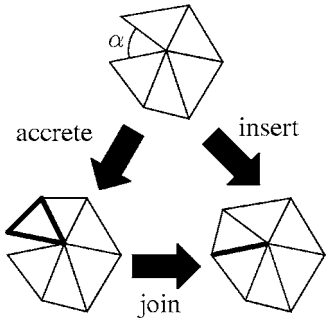

FIG. 2. Elementary growth steps of *insertion, joining*, and *accretion*, performed from the same starting point of an edge with opening angle α. Insertion can be decomposed into accretion followed by joining.

Given a set of connected triangles (a topological configuration), we can now use this Hamiltonian to determine the lowest-energy configuration of the positions of the triangles. These positions correspond to a continuous degree of freedom which is now fully determined by the model ($\mathcal{H}$) and the connectivities—the discrete degree of freedom. Ultimately, we are only concerned with the discrete configuration.

C. Growth

We have noted that capsids are determined by the locations of the disclinations (pentamers). For an irreversible growth model, in which no step can be undone, the fundamental question is therefore: while growth occurs at the border, which twelve vertices are frozen in as pentamers? Keeping this in mind, we will now discuss our capsid growth process.

1. Growth steps

We define transitions between incomplete capsids, consistent with irreversible growth, called *growth steps*. Two elementary growth steps are immediately apparent: *accretion* and *joining*. Accretion is the addition of a single triangle to a border edge and joining is the formation of a bond between two adjacent border edges. We require the vertex between these two joined edges to have five or six triangles around it in order to ensure that only pentamers and hexamers form.

Besides accretion and joining, we define a third, composite growth step: *insertion*. We define insertion as accretion followed by joining along an edge of the new triangle. The vertex into which we insert must have four or five triangles. Insertion at a four vertex or joining at a five vertex is the only way to form a pentamer. These three steps are illustrated in Fig. 2.

Growth begins with a small template—either a single triangle or a pentamer of five triangles about a vertex. From here, the growth is determined by the sequence of growth steps, which is chosen stochastically. We will first present our rules for the relative probability of choosing the growth steps, and then explain their microscopic rationalization.

2. Rates

We precede each growth step by relaxing all vertex positions using a conjugate-gradient algorithm to minimize the positional energy $\mathcal{H}$. Now a rate k_ν is defined for each allowed growth step ν, which is a function of the local topology and of the *opening angle* α between pairs of edges at each vertex on the border, defined in Fig. 2. The probability of step ν is then taken to be $k_\nu/\Sigma_\mu k_\mu$; once a step ν is picked, we perform the step and iterate the process (beginning as before with a relaxation).

We take the accretion rate k_A to be independent of the local configuration: in particular, it is not a function of α.

So long as we are concerned only with the outcome and not the time taken to reach it, only relative rates are relevant. Thus we can now define

$$\frac{k_J(\alpha)}{k_A} = \Gamma_J e^{-\alpha^2/2\sigma^2}, \tag{8}$$

$$\frac{k_I(\alpha)}{k_A} = \Gamma_I e^{-(\alpha-\pi/3)^2/2\sigma^2}, \tag{9}$$

with justification to follow. Note that steps are only considered if (1) they do not break any topological rules by enclosing a vertex with other than five- or sixfold coordination, and (2) they do not lead to steric hindrances. This second point is discussed further in Appendix B.

3. Microscopic justification of rates

While many models explicitly account for units in solution and fluctuations in incomplete capsids [22,46], we have chosen a simplified cartoon model. Implicit to this is the idea that the capsid is thermally fluctuating between growth steps.

Say the time between successive additions is longer than the relaxation time scale of the positional degrees of freedom. Then between each growth step, we can assume that the incomplete capsid is in equilibrium and thus samples a Boltzmann distribution. We consider the energy of fluctations about the relaxed position. For a particular vertex i, with a relaxed opening angle α_i, the energy of a fluctuation with opening angle $\alpha_i+\Delta\alpha_i$ is well approximated by a quadratic, so that

$$\Delta E(\Delta\alpha_i) \approx \frac{1}{2}A_i(\Delta\alpha_i)^2. \tag{10}$$

We can therefore determine the elastic energy barrier for a vertex to have an angle favorable for either insertion ($\alpha_i+\Delta\alpha_i \approx \pi/3$) or joining ($\alpha_i+\Delta\alpha_i \approx 0$), and thus the transition rates, $k_I(\alpha_i)$ and $k_J(\alpha_i)$, respectively (Fig 3). It is now clear that the rates defined above in Eqs. (8) and (9) are merely Arrhenius factors, with

$$\sigma^2 = \frac{k_B\mathcal{T}}{A_i}. \tag{11}$$

where $\mathcal{T}$ is temperature.

During any growth step, new bonds are formed. We may consider an extra energy term, $\mathcal{H}_{\text{bind}}=-N_bE_b$, contributing a binding energy $-E_b$ for each of the N_b bound edges in the capsid. Such an energy is independent of the positional configuration. For our irreversible model to satisfy detailed balance, we need $E_b \gg \Delta E(\Delta\alpha_i)$ so that the energy barrier for the reverse transition is large compared to that for the forward transition.

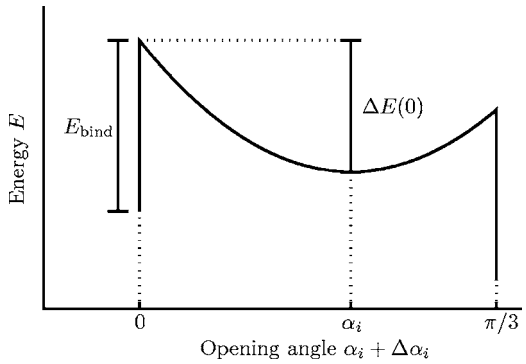

FIG. 3. A representation of the energy as a function of opening-angle fluctuations $\Delta\alpha_i$. When $\alpha_i+\Delta\alpha_i$ reaches either 0 or $\pi/3$, we imagine joining or insertion, respectively, occurring, reducing the total energy by E_{bind} for joining, and some combination of E_{bind} and a chemical potential for insertion.

The parameter A_i and therefore σ depends not only on the elastic constants, but also on the local environment of the vertex in the capsid. We can determine normal values for A_i by varying angles on different capsids with different energy parameters, and twice differentiating the Hamiltonian about the minimum. Because most of the opening angle fluctuations in physical situations are *in plane*, A_i depends most strongly on the Young's modulus, and generally

$$A_i = \frac{\partial^2\mathcal{H}}{\partial\alpha_i^2} \approx 0.1\tilde{Y}r_0^2. \tag{12}$$

(Note that this is an absolute dependence on the energy scale $\tilde{Y}$, and is the only reference we will make to an absolute energy, since everything else depends only on the ratio $\tilde{\kappa}/\tilde{Y}=\ell_f^2$.)

We can perform a rough estimate of this width σ. Using the elastic parameters estimated for *fd* in Sec. II B, and assuming $r_0 \approx 4$ nm, we find $A_i \approx 0.1Yr_0^2 \lesssim 17$ eV. We therefore expect fluctuations of

$$\sigma = \sqrt{\frac{k_B\mathcal{T}}{A_i}} \gtrsim 0.038 \approx 2.2^\circ \tag{13}$$

at room temperature. We will need $\sigma \gtrsim 10^\circ$ for satisfactory growth—a reasonable possibility considering that we conservatively ignored bending rigidity and charge. Had we performed this estimate using the much larger value of Y from $\phi 29$, we would find fluctuations an order of magnitude smaller, leading to a regime in which growth is not feasible. But the $\phi 29$ measurements were taken from the head of a mature bacteriophage, which is observed to be much more faceted (small ℓ_f, large Y/κ) than the immature form in which assembly occurs. Such small fluctuations are probably important for stability and infectivity, but also quite detri-

mental to growth [57]. As such, we expect the immature capsid to have much larger fluctuations, although no mechanical studies have been done to allow this determination.

Sometimes a deterministic growth rule is preferred to the stochastic rule presented above. One possibility is a rule that accepts only the move with the largest rate at any given point.

III. FAILURE MODES

The restriction that all vertices have either five or six triangles can lead to problems in irreversible growth. It is entirely possible for a growing capsid in our model to perform a wrong growth step resulting in a state which can never be completed—that is, no complete capsid satisfying the pentamer/hexamer-only requirement includes the particular incomplete capsid in any of its possible growth histories. This section surveys two common failure modes. A common theme is that the failure can be identified nonlocally, long before a step is reached at which the growth rules break down; a more rigorous treatment is given in Appendix A.

We cannot avoid considering failures, since we must exclude them when reporting statistical distributions of the resulting capsid ensemble (see Sec. IV). More importantly, we have taken for granted that actual physical assembly has a high success rate (say, 10% to 99%). Indeed, most of our labor on the project reported in this paper consisted of locating the region of parameter space in which assembly had a high success rate. Classifying the failure modes is a prerequisite to understanding what conditions reduce or eliminate them.

Failure modes are also experimentally pertinent. Whatever the "ideal" capsid is for a given virus species, there is likely to be more than one possible assembly model that produces it. But since different models will tend to fail in different ways, they are better distinguished experimentally by the study of defective rather than of ideal capsids. If there are virus species that grow their capsids near the limit of complete irreversibility, the resulting ensemble is bound to contain mistakes. Indeed, HIV cones have been observed that are surrounded with what is believed to be a second complete sheet of capsid protein [33].

A. Unfillable quadrilateral hole

First we look at a failure that occurs only at the end of a growth process. Figure 4(a) shows a common configuration with a single quadrilateral hole. Parallel transporting a vector around the border gives no rotation and therefore there is no net disclination inside (the net "disclination charge" is zero—recall the discussion in Sec. II A). The only conceivable filling is with two triangles, but either possibility introduces a seven-coordinated vertex [58].

A less trivial example of this situation is shown in Fig. 4(b). Here we can parallel transport a vector around the border to see that a single disclination must reside within the border; however, there is no way to fill in the remaining triangles to satisfy this. See Appendix A for a more rigorous discussion of this phenomenon. If we continue growth, the hole will eventually shrink to something similar to Fig. 4(a). Some believe that such a hole is not detrimental to capsids, and in fact capsids are suspected to be permeable to water and ions. On the other hand, HIV is known to have a particle-to-infectivity ratio on the order of 100 [59], and such holes, if they are very common and detrimental to infectivity, may explain why 99% of virions are not infectious.

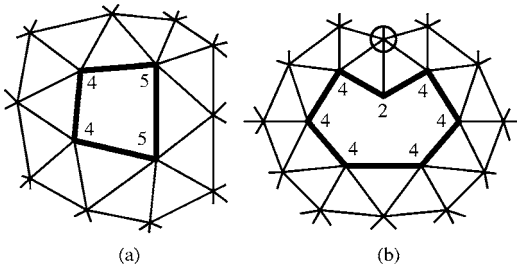

FIG. 4. Incompletable holes at the end of growth. Neither hole can be filled without introducing a heptamer. The hole in (b) would have been avoided had the circled vertex been made a pentamer.

This type of failure was common in all the growth rules we considered, although it is more prevalent in certain situations. In particular, if the growth rate parameters defined in Eqs.(8) and (9) are large, $\sigma \gtrsim 20$ or $\Gamma_{I,J} \gtrsim 200$, then creation of pentamers becomes very random and is no longer based on the configuration. In normal growth, particularly at small ℓ_f (angular regime), local strains cause angles along the border to suggest whether a pentamer or hexamer should be created, but large σ decreases the sensitivity to this.

B. Crevice formation

Next we look at a failure that can occur at any point during the growth, called a *crevice*. We see in Fig. 5(a) a portion of a border with the four labeled vertices in a characteristically incompletable configuration. This becomes clear when the border is flattened onto a reference lattice, as seen in Fig. 5(b). We now see that in the absence of pentamers in the neighborhood of this section of border, several triangles lie on top of others. The introduction of a pentamer can only make matters worse. By effectively cutting out a

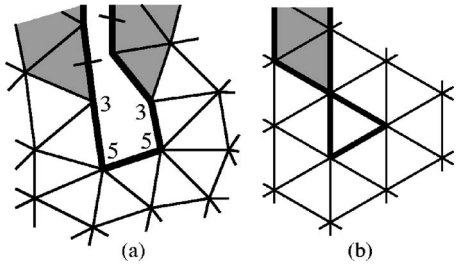

FIG. 5. (a) An incompletable configuration. The sequence of vertices with 3, 5, 5, and 3 triangles on a border can never lead to a valid complete capsid. Joining the marked edges would produce an unfillable quadrilateral hole, similar to Fig. 4(a). (b) The same border flattened onto a triangular reference lattice. The shaded triangles from (a) now overlap the corresponding triangles from the opposite side.

60° section of the plane, it becomes even more crowded. The only way to alleviate this self-intersection is by introducing a negative disclination (heptamer).

Crevice failures can occur in different regimes, but arise, in particular, during *fingered* growth. If accretions are much more common than both joinings and insertions (such is the case when either $\sigma \lesssim 5°$ or $\Gamma_{I,J} \lesssim 1$), then we expect many long fingers only one or two triangles wide. Crevices occur easily between these fingers. Even in the absence of fingers, sometimes creating a pentamer will distort a neighboring vertex enough that the angle is too large for insertion or joining. This too often results in a crevice.

Say a single crevice failure occurs during growth. Further growth outward from the failure should be prevented by steric hindrance. But growth elsewhere along the border will continue and eventually fill in the crevice from its far end. Then the capsid will almost complete, leaving a small hole of the same type discussed in Sec. III A above. The two marked edges in Fig. 5(a), for instance, might eventually join, leaving a quadrilateral hole.

If two or more crevice failures occur, however, our model's resulting capsid will have a network of cracks connecting these failures. Real capsids might repair this problem by binding edges not sharing a vertex (which is forbidden in our model); in that case, the final result might instead have several small quadrilaterals of the type seen in Fig. 4(a).

Although it is not as obvious, the smaller holes presented in Sec. III A also have borders whose flattened images intersect themselves when cut at certain places. We can generalize this by stating that a border is incompletable if there is any choice of cut that leads to any triangles along the flattened border intersecting one another. The converse is true in most cases as well.

C. Failure rates

If fivefold vertices were simply incorporated at random moments during the growth, virtually every capsid would fail in one of the two modes described in this section. Since the topological constraints to be satisfied are nonlocal, and the growth rates depend on local properties, it seems mysterious at first how the growth can be as successful as it is. The key is that, in an elastic medium, the strain due to a defect (such as a disclination) is also nonlocal; at least, it decays as a power law with the distance from the defect. In this fashion, the necessary information about the location of a faraway disclination is passed to the growth border.

Since growth is stochastic, there is a possibility of errors despite this passage of information. All capsids are in danger of making an error after the eleventh disclination is in place, and many are in danger even earlier.

We can model the failure probability with a very simple assumption: each time a triangle is added, there is a fixed probability $p_c \ll 1$ of starting a crevice. This is not intended quite literally: p_c must be understood as the fraction of edges along the border that can possibly start a crevice, multiplied by the probability on each such edge that this "wrong" step will be taken when a triangle is added there. (The crucial step might be a "joining" but this contribution gets folded in with the other one, since the border settles into a dynamic near-steady state, so that the ratio of step types will be uniform on averge.)

The survival probability of a defect-free capsid is thus

$$\frac{dP_{\mathrm{sur}}}{dN} = -p_c, \tag{14}$$

where step N plays the role of time, so that

$$P_{\mathrm{sur}}(N) = P_0 e^{-p_c N}. \tag{15}$$

Growth will terminate after all twelve disclinations have been incorporated, i.e., on average when $N=\bar{N}(\theta_0, \ell_f)$ (the mean size of capsids formed as a function of the parameters). Furthermore, we hypthesize that $p_c \approx p_c(\ell_f)$, i.e., crevice formation depends strongly on the ratio of elastic constants and almost not at all on the preferred angle θ_0. If so, the probability of success is

$$P_{\mathrm{succ}} = P_{\mathrm{sur}}(\bar{N}) = e^{-p_c \bar{N}}. \tag{16}$$

Indeed, we will see the dependence of p_c and P_0 on ℓ_f in Sec. IV B.

IV. RESULTS

Here we discuss several measurements that can be used to quantitively characterize various properties of capsids (individually, or as an ensemble) specified by a triangulation of vertices, such as the results of our growth model. Our results fall into three general categories: size, success, and shape. First, we look at the size of the resulting capsids and show the dependence on the elastic parameters. Next, we look at the probability of successful growth, in terms of both the size of the capsid and of the growth-rate parameters. Last, we comment on measures of capsid shape, which, along with capsid size, is a measurement that can be used with data from cryo-EM experiments.

Figure 1 shows an example of a typical capsid shell resulting from our growth simulation. This capsid emphasizes that our configurations are inherently random and irregular. The degree of "lumpiness" in the external shape depends strongly on the Foppl–van Kármán length ℓ_f, as is elaborated in Sec. IV C, below.

Each capsid is grown until either a successful completion or an identifiable failure, such as a self-intersection in the flattened border. Relaxations are minimized until the gradient squared is less than 10^{-6} in units with $K_{\mathrm{stretch}} \geq K_{\mathrm{bend}} = 1$. The entire growth process for a small capsid takes several minutes on a 1.6 GHz processor, while a large capsid takes many hours, the majority of the time devoted to minimizing energy. The following plots of size and success rate include data from 134 352 capsids.

A. Size

The simplest thing to observe about a capsid is its size. We can count the number of triangles N, or measure the average radius R. As expected [13,16], capsid size depends most heavily on two parameters from our effective Hamil-

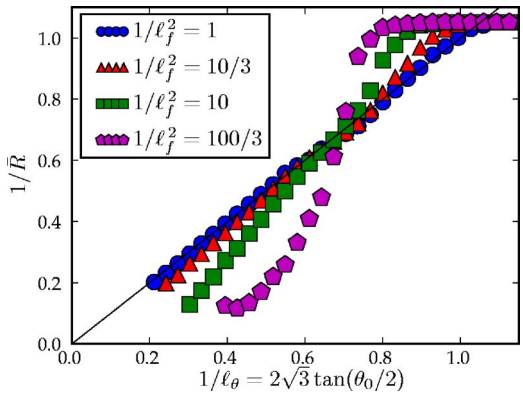

FIG. 6. (Color online) Plot of $1/\bar{R}$ vs $1/\ell_\theta = 2\sqrt{3}\tan\theta_0/2$, in units of r_0. We see that in the smooth regime of small $1/\ell_f$, the mean capsid radius $\bar{R}$ very nearly follows ℓ_θ. In the angled regime (large $1/\ell_f$), we find smaller capsids (many $T=1$) for a much larger range of $1/\ell_\theta$, followed by a sharper increase in size at smaller cunrvatures. Parameters with fewer than ten successful capsids were omitted.

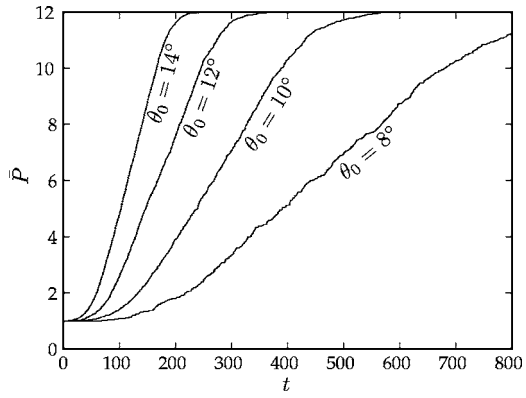

FIG. 7. Plot of the average number of pentamers $\bar{P}$ vs the step number t, which is nearly equivalent to the number of triangles N. This gives a picture of the general pathway of growth behind the curves in Fig. 6. This growth was carried out at $1/\ell_f^2 = 10/3$, and different spontaneous curvatures θ_0 as shown in the figure. We see that growth consists of an initially slow process to add the second pentamer, followed by a rather linear regime in which $d\bar{P}/dN$ is roughly constant. Note that both the initial rate at $P=1$ and the following slope depend on ℓ_f.

tonian, $\ell_f = \sqrt{\kappa/Y}$ and θ_0, which we rewrite as a length

$$\ell_\theta \equiv \frac{r_0}{2\sqrt{3}} \cot(\theta_0/2). \tag{17}$$

This length is the radius of curvature from two equilateral triangles with side length r_0 joined at an angle θ_0 and tangent to a common sphere. We now have three length scales, r_0, ℓ_θ, and ℓ_f. It is useful to think of these as two dimensionless parameters, $1/\ell_\theta$ and $1/\ell_f$, taking $r_0 = 1$.

In the smooth regime, when $1/\ell_f \lesssim 50/\ell_\theta$, the variation in the dihedral angles at different bonds is small, so the radius of the resulting capsids approaches ℓ_θ. For larger $1/\ell_f$ (the angled regime), the Young's modulus increases. Hexamers, which make up most of the capsid, become flatter. Thus, the effective preferred angle θ_0^{eff} decreases, resulting in larger capsids.

We simulated many capsids assembling at four values of $1/\ell_f$ and θ_0 between 7° and 36°. For each set of parameter values, we averaged the radius of the completed capsids, $\bar{R}$, and plot the inverse of the radius $1/\bar{R}$ as a function of the spontaneous curvature $1/\ell_\theta = 2\sqrt{3}\tan(\theta_0/2)$ in Fig. 6 for several different values of ℓ_f. We see that, for large ℓ_f, the curves roughly follow the line $1/\bar{R} = 1/\ell_\theta$. As ℓ_f decreases, we see a very different behavior, which favors small (mostly $T=1$) capsids for a much larger range of θ_0, before the size suddenly increases very quickly around $1/\ell_\theta \approx 0.7$. We can see what is behind these curves in Fig. 7, which shows the average growth history for several individual parameters, represented by the average number of pentamers $\bar{P}$ as a function of the number of growth steps t.

B. Success rate

An important consideration for an irreversible growth model is under what circumstances it successfully produces complete capsids. We have already shown that a variety of failure modes exist, resulting in incompletable capsids. We can easily quantify how often these failures actually occur as a function of parameters. We predicted in Sec. III C that the success rate should be exponential with the expected size of the capsid. For each choice of parameters, we average the sizes (measured by the number of triangles, in contrast to radius as in Fig. 6) of the capsids, and thus map the parameters θ_0 and ℓ_f to $\bar{N}(\theta_0, \ell_f)$. We then plot the percentage of capsids that completed successfully when grown with these parameters in Fig. 8. While there is systematic deviation from exponential decay, due to the many considerations left out of our analysis, we do still see a mostly exponential trend in the data.

We see in Fig. 8 that for a given size, growth is generally more successful for more faceted capsids. For large capsids (best-fit radius $\bar{r} \gtrsim 10 r_0$), the failures in the smooth regime ($1/\ell_f^2 \leqslant 10/3$) all occurred in the early stages of growth, in

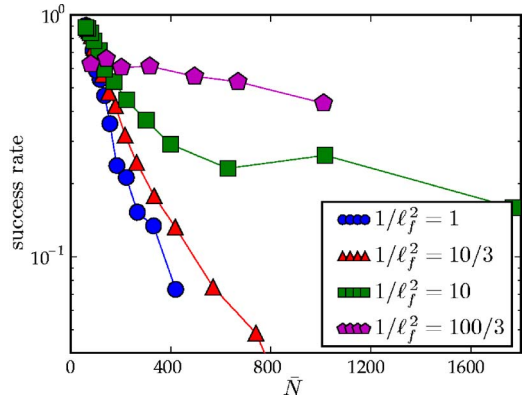

FIG. 8. (Color online) Plot of success rates as a function of $\bar{N}$ for the given parameters, from the size measurements. We see a somewhat exponential decay, suggesting that the introduction of errors is a Poissonian effect, as discussed in Sec. III C.

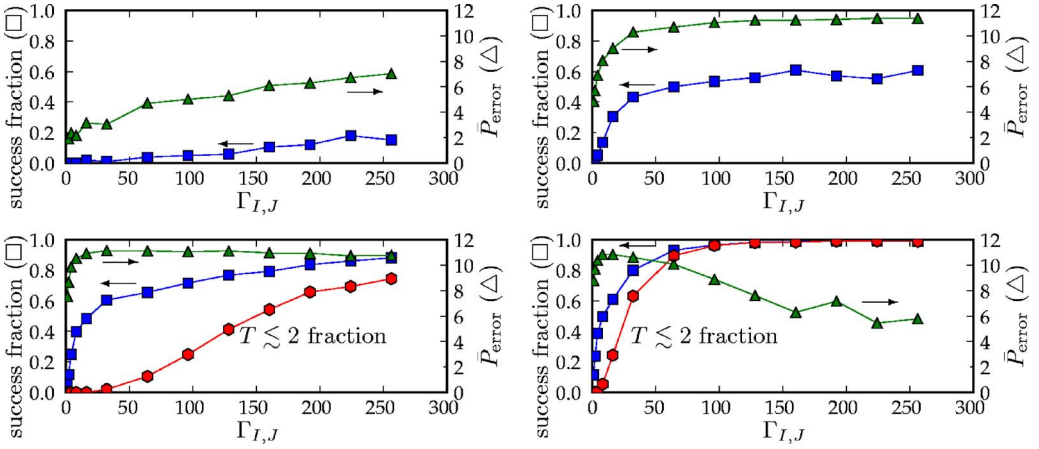

FIG. 9. (Color online) Success fractions as a function of rate parameters $\Gamma_{I,J}$ and σ ($\sigma=8°$, top left; $\sigma=12°$, top right; $\sigma=16°$, bottom left; $\sigma=20°$, bottom right). The square markers show the fraction of successful capsids at each parameter, including small capsids. For $\sigma=16°, 20°$, the hexagons mark the fraction of total capsids, which were small (successful and less than 46 triangles, or pseudo-$T \lesssim 2$). The smaller values of σ had no such capsids. Finally, the triangular markers show the average number of pentons $\bar{P}_{\text{error}}$ at the time of error detection. Note that $\bar{P}_{\text{error}} \to 12$ means that all the errors are small holes at the end of growth.

which only a few pentamers had been added. This suggests that large bending stiffnesses lead to more common crevice failures. On the other hand, the faceted capsids ($1/\ell_f \geq 10$) failed mostly in the late stages, in which only several pentamers were missing, suggesting that faceted capsids are somehow resistant to crevice failures and instead fail with small holes.

In Sec. III, we mentioned the impact of the rate parameters $\Gamma_{I,J}$ and σ on successful completion. We measured the failure rate as a function of these parameters, using reasonable values of $\theta_0=16°$ and $\ell_f^2=0.1$. In Fig. 9 we plot the fraction of failed capsids due to either small holes at the end of growth, or crevice failures in the middle of growth. We see that small values of $\Gamma_{I,J}$ and σ indeed produce errors. Larger values of σ and $\Gamma_{I,J}$ produced successful capsids, but almost all were $T=1$. This particular result is very sensitive to our particular growth rules, and a choice that prevented insertion until there were five triangles around a vertex would drastically change the result.

C. Shape

Beyond size and success, most other measurements fall under the category of shape measurements. In particular, we might measure either the degree of symmetry or the facetedness of a capsid.

Spherical harmonics may be useful for evaluating icosahedral symmetry, as spherical harmonic coefficients of icosahedrally symmetric functions vanish for all but $\ell=0,6,10,\ldots$.

Kingston *et al.* [35] uses the asphericity, defined as the ratio of inradius to circumradius to measure the faceted shape of RSV capsids. Lidmar *et al.* [20] also defined an asphericity, $\langle R^2\rangle/\langle R\rangle^2$. While these are good measurements for symmetric capsids, they are not useful for the irregular capsids we grow because they cannot distinguish between, for instance, a smooth egg-shaped capsid and a faceted spherical capsid. We instead use a measure based on the Gaussian curvature, described below.

1. Curvature

In light of recent advances in tomography, a very relevant measure is Gaussian curvature K. In our discrete triangular model, we can measure the integrated Gaussian curvature $I=\int K da$ over the neighborhood nearest to a single vertex by measuring the area (equivalently, angle surplus) of the spherical polygon traced out by the incident triangles' unit normals. We can easily extend this to the integrated curvature over all the vertices within any loop around the capsid. The integrated curvature over the entire capsid is always 4π, a topological invariant related to the Euler characteristic. The question then arises how this curvature is distributed over the capsid. For highly faceted capsids, each pentamer has $I \sim \pi/3$, while the rest of the capsid has $I \to 0$. On the other hand, the curvature is distributed uniformly over smooth capsids. This motivates the definition of an inverse participation ratio (IPR)

$$P = \frac{\left(\sum_j I_j\right)^2}{\sum_j I_j^2} = \frac{(4\pi)^2}{\sum_j I_j^2}, \tag{18}$$

where I_j is the integrated curvature about vertex j. This essentially measures the number of lattice sites the curvature is localized to. The IPR is plotted for a single capsid relaxed to different elastic parameters in Fig. 10. We see that $P=12$ at $\ell_f \to 0$ while $P \to N_{\text{vert}}$ at $\ell_f \to \infty$.

This same integrated curvature can be measured on triangulated tomographical data from capsids. The integrated curvature within large loops should be relatively stable even if the Gaussian curvature varies quickly. For an arbitrary loop around a capsid, we will get a contribution of $\pi/3$ from each enclosed pentamer. The loop may then be pulled tighter to pinpoint the location of each pentamer. We simulated this

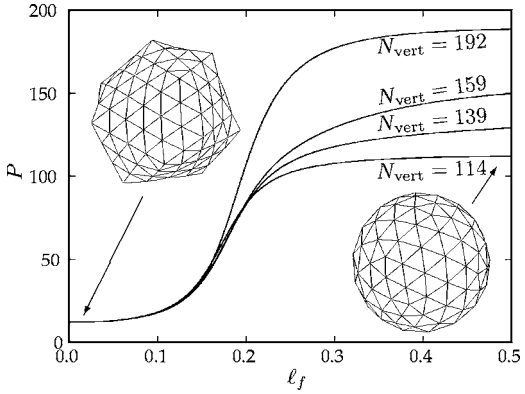

FIG. 10. Inverse participation ratio for four capsids with different numbers of vertices N_{vert}. We can see that at $\ell_f=0$ (the angular limit), $P=12$, and as ℓ_f increases (the smooth limit), $P \to N_{\text{vert}}$. The exact shape of the curve depends on the placement of pentamers, but in general we see an inflection point around $\ell_f=0.18$, which corresponds to $\gamma=R^2/\ell_f^2$ roughly between 200 and 400.

process by growing a large number of random capsids and integrating the curvature within many random loops on each. Each capsid was relaxed to several different values of ℓ_f. The resulting distribution of curvatures is displayed in Fig. 11. At large $1/\ell_f \approx 20$ we see very sharp peaks. These peaks diffuse into a mostly uniform background by $1/\ell_f \approx 2$.

2. Average dihedral angle

We can measure the average dihedral angle of either a growing or a complete capsid. Figure 12 shows a graph of the average dihedral angle for a very large pentagonal sheet with a single disclination in the center as a function of ℓ_f, at different θ_0. We see a first-order phase transition at $\theta_0=0$.

V. DISCUSSION

In this section, we recapitulate the highlights of our model and the simulation results, and outline extensions that could improve their realism.

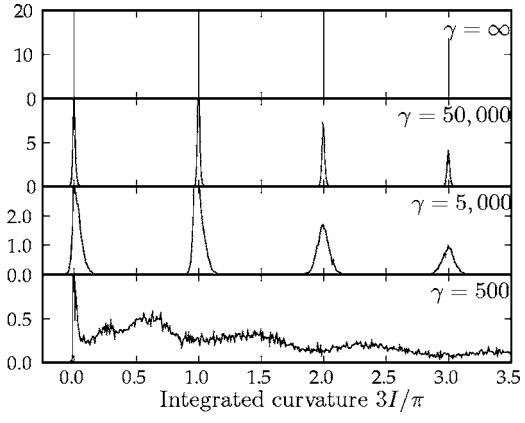

FIG. 11. Distribution of integral curvatures within random loops around random capsids relaxed to four different elastic parameters, characterized by $\gamma=(R/\ell_f)^2$. The distribution is sharply peaked at the integers for the angled regime at small ℓ_f and diffuse for the smooth regime at large ℓ_f.

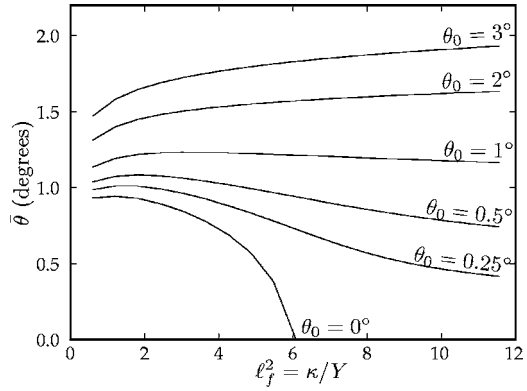

FIG. 12. Average dihedral angle of a large pentagonal sheet with a single disclination in the center. Plotted vs ℓ_f at different θ_0. The bottom $\theta_0=0$ curve shows a first-order buckling phase transition. Each subsequent curve increments θ_0 by 0.25°.

A. Summary of results

Our irreversible growth model, based on trimer units with the simplest possible Hamiltonian and growth rates, did succeed at producing closed capsids, but only when the parameters are tuned to the proper range: $1/\ell_f \lesssim 10$, $\theta_0 \gtrsim 8°$, $\Gamma_{I,J} \gtrsim 50$, and most importantly, $\sigma \approx 12°$.

Our model (Sec. II) made a sharp division between configuration variables that were continuous (position) and discrete (bonding topology); correspondingly, the model parameters were divided between a Hamiltonian (harmonic form) and rate constants for a set of first-order processes; for simplicity, monomers in solution were not treated explicitly. The model's most distinctive feature is its use of trimer units (triangles), which turns out to have several inherent disadvantages. First, our "insertion" step (Sec. II C) seems as though it should be redundant; unfortunately, omitting this (relying on the "joining" step in its stead) produces abundant failures—the fingered growth and crevices discussed in Sec. III B. In other words, good growth depended on joinings being rare compared to insertions, which followed from our growth rules (Sec. II C), since opening angles α near 0° are much less common than those near 60°. This may mean that if a capsid assembles from trimers in solution, the only way to have normal growth is that there must be cooperative binding as in our insertion step.

Our results may be divided into two categories: the growth process (including the success rate) and the shape of the resulting model capsids. In the first category, we found mathematical descriptions (Appendix A), which clarified the constraints on the positions of the fivefold-coordinated vertices, which fully characterize the bond network. Additionally, we uncovered a simple relation between the chance of failure and capsid size, Eq. (16). In the second category, we showed the relationship between the capsid's final size and the two length parameters ℓ_f and ℓ_θ. In contrast to Nguyen *et al.* [38], we note that the *average* capsid size is indeed well determined by the spontaneous curvature parameters for large capsids, even in the absence of any scaffolding considerations. We also extended the concepts of Ref. [20] to irregular capsids. In particular, the ratio of bending and

stretching stiffnesses—which we suggest is best parametrized by a length, Eq. (5), rather than a dimensionless ratio—controls whether the resulting shape is smooth or angular, as we have characterized by an inverse participation ratio, Eq. (18).

One application of our results from different ℓ_f relates to phage maturation. Many phages include a maturation step in which the assembled prohead greatly increases its stretching stiffness relative to its bending stiffness, making it more faceted. One might ask why the assembly process occurs in the smooth regime, especially since our results in Sec. IV B show that the probability of success is smaller in this regime. We propose that the advantage of growth in the smooth regime is size selection. In Fig. 6 we see that faceted capsids have a sharp transition in size around the region most phages fall into ($T=3$ to $T=7$). As might be expected, for a given set of parameters, the spread of capsid sizes is also much broader near this transition. Thus, in order to well control the size of assembled capsids, a virus might prefer to grow in the smooth regime, counting on other factors such as scaffolding to increase its chances of successful assembly.

B. Future directions: More realistic random growth

1. Models with nontrimer units?

The retroviral CA proteins we claim to model have well-documented dimerization [60] and hexamerization [61] interactions, but no trimer interactions have been observed in retroviral capsids. A model based instead on pentamers and hexamers could be implemented simply by changing the growth steps to add several triangles at a time, so as to fully enclose a single vertex each step into either a hexamer or a pentamer. We gain some benefit, however, from actually changing our representation to a honeycomb lattice—the dual to our current triangular lattice. Vertices of the dual lattice are all three coordinated, so each vertex along the border has either one or two capsomers attached to it—much simpler than the five different possible coordination states for border vertices in the trimer model. In this model, growth rules could explicitly depend on the total coordination of a vertex. Such coordination-based rules greatly assisted successful growth in our trimer model, but were not as physically justifiable as they are in the dual model.

These considerations suggest that behavior arising from this choice is not universal. We expect models based on dimers, trimers, or pentamers and hexamers to fall into different universality classes.

Another direction leading to a more realistic model is to improve the accuracy of our interactions. Microscopic electrostatic simulations, such as with the CHARMM software, could provide a more realistic Hamiltonian for specific viruses, which could be included in future models.

2. Lattice fluctuations

A deeper understanding of the relationship between topological configurations is critical. So far we have only thoroughly considered irreversible growth transitions. Other transitions relate to the motion of disclinations on the lattice (always in pairs), both for the purpose of enumerating the near-symmetric states, and for an understanding of the rearrangement dynamics by which real capsids may anneal their bond configurations into the free-energy minima predicted by many equilibrium models.

C. Future directions: Realistic shapes

All well-studied real capsids exhibit greater regularity than our current model can regularly generate. How can the Hamiltonian (or the growth dynamics) be modified so as to generate an icosahedral, or (for HIV) conical capsid?

1. Icosahedral symmetry

The main challenge for theory is to explain the assembly of icosahedrally symmetric capsids, if one is not close to equilibrium. Hamiltonians such as ours do indeed give effective repulsion between the disclinations, and the free-energy minimum is known to have icosahedral symmetry in similar models [13,20]. However, this is simply insufficient to produce large symmetric capsids in a model where the accretion rate depends on local geometry, since the growing border does not contain enough information in just the opening angles (Sec. II C). Even deterministic variants of the growth model never yielded icosahedral capsids larger than $T=4$.

We speculate that if the bending potential $\mathcal{H}_{\text{bend}}$ was not simply harmonic around θ_0, but instead had minima at two different angles θ_1 and θ_2, this might robustly favor a regular pattern of edges with θ_1 and θ_2, thus permitting the determination of larger icosahedral capsids. A double-well potential would presumably represent some sort of conformational switch, perhaps an internal bending between two domains of the capsid protein. Thus, this proposal has some features in common with the matching-rule models that we dismissed as implausible (Sec. I B), but anharmonic potentials seem much more natural than variations in the edge binding (which, in our model, corresponds to the term $\mathcal{H}_{\text{bind}}$ mentioned briefly in Sec. II B).

One other change, which could result in more symmetric capsids, as well as more successful growth in general, is to relax our irreversibility constraint. Allowing the growing edge to "melt back" would allow a growing capsid to better explore the possible configurations, in particular, curing crevice and fingering defects.

2. Retroviruses

We asserted that the randomness of our model's growth behavior makes it appropriate for modeling the irregularity and pleiomorphism observed in the capsids of retroviruses such as HIV. However, mature HIV capsids do have a typical gross shape, which is mostly conical (although sometimes tubular) in vivo, whereas our current model grows round capsids on average. A cone is charaterized by having (say) five disclinations around its smaller end, seven around the large end, and none on the belt between; this means the rates of adding pentons must somehow vary during different stages of the growth. When cones form inside an envelope, the difference could be attributed to the depletion of the monomers as they are incorporated into the capsid: that (see

Sec. II C) would decrease the rate of insertion but not of joining, leading to a greater chance of penton formation. A difficulty with concentration control is that cone completion leaves in solution 70% [29] of the capsid proteins: in order for this to grossly affect the rates, accretion must microscopically be a rather high-order process. It also leaves unexplained the large density of pentons at the *earliest* stage: a possibility is to add a simple interaction between the capsid and either the nucleic acid or the membrane [33,32].

ACKNOWLEDGMENTS

We would like to thank John Briggs for access to his unpublished work, and Robijn Bruinsma, Grant Jensen, Diana Murray, and particularly, Volker Vogt for many discussions. Our interest originated in the suggestion of B. Shraiman, who pursued similar growth simulations on the aggregation of clathrin cages [62] and on virus capsids [63]. This work was supported by U.S. Department of Energy Grant No. DE-FG02-89ER-45405.

APPENDIX A: COMPLETABILITY

It is possible to grow an incomplete capsid that is not part of any allowed capsid. This appears to be a consequence of our rule that a capsid vertex can only have coordination five or six. (Seven-coordinated vertices, were they allowed, would let the capsid recover from almost every "mistake" discussed in this section.)

As a complement to the more qualitative discussion in Sec. III, this appendix presents the technical criteria we discovered to identify when a partial capsid is or is not completable, nonlocally and long before the growth rules carry us to a point where we must make a sevenfold vertex or stop. The completability conditions are defined entirely in terms of the growing border, which can be uniquely described by traversing the vertices (in a specified direction) and listing the number of triangles present at each vertex. Thus a string of numbers from 1 to 5 specifies a border. (6 is allowed, but is trivial.)

1. String representation

We can represent any border by a word $a_1 a_2 \cdots a_n$, where $1 \leqslant a_i \leqslant 6$ is the number of triangles around the ith vertex, counting clockwise from an arbitrary starting point. We define several operations on these string representations. First, consider

$$A(a_1 a_2 \cdots a_n) \equiv 1(a_1+1)a_2 \cdots (a_n+1) \tag{A1}$$

and

$$J(a_1 a_2 a_3 a_4 \cdots) \equiv (a_1+a_3)a_4 \cdots, \tag{A2}$$

representing accretion and joining, respectively. Note that the a_2 term disappears upon applying J. This vertex is enclosed and is no longer part of the border. We therefore require $a_2 = 5$ or 6. We can further define insertion $I=J\circ A$ as the composition of joining and accretion. Finally, because we defined these operations to act on the starting and ending points of our string representation, we must define a cycle operation, $C(a_1 a_2 \cdots a_n) \equiv a_2 \cdots a_n a_1$. Because of the unimportance of the starting point in representing a border, cycling leaves borders invariant. Since these operations are sufficient to grow any capsid, we can uniquely describe a capsid by the sequence of operations on the border required to arrive at the border from a single triangle, 111.

Using this representation we can immediately identify some borders that are incompletable. Consider the border $X = 555\cdots$. Joining is illegal since it leaves a vertex with ten triangles. Accretion leads to $A(X)=6166\cdots$, which clearly cannot be completed since only joining can be done on the 6's, and this leaves seven triangles at least one vertex. Finally, insertion yields $I(X)=66\cdots$, which is incompletable for the same reason.

Any border that intersects itself on a flat reference lattice is incompletable (coincident edges are allowed). It is important to take notice of which side of the border is the inside (from which the triangles are being counted) and which is the outside.

We thus define the complement of a border,

$$\overline{a_1 \cdots a_n} \equiv (6-a_n) \cdots (6-a_1). \tag{A3}$$

If the original border enclosed d disclinations then its complement encloses $12-d$ and can be glued together to form a complete capsid. We must note two things. Firstly, the complement of a border may be a border that cannot possibly be grown using our growth operations. Secondly, the complement is only unique insofar as the seam between the two incomplete capsids is occupied only by sixfold vertices. However, many "pseudocomplements" may be constructed, which leave disclinations on this seam.

While the border by itself is useful for analyzing completability, it does not uniquely describe the interior. An individual border may have many different realizations, with disclinations in different positions. In fact, a pair of disclinations can move in opposite directions (relative to a common reference lattice, if one exists) without changing the border.

2. Winding number

We can compute the winding number $W(a_1 a_2 \cdots a_n) \equiv \Sigma_i (a_i - 3)$ of a border, which is the number of 60° turns undergone by a direction that is parallel transported about the border. The total net number of disclinations within the border is $W+6$. If we allowed sevenfold disclinations, they would be subtracted from this number. Since we only allow single positive disclinations, we can conclude that the winding number around any path on a valid capsid must be between −6 and +6, leaving $6-W$ disclinations which must be placed in the unfilled part (the other side of the border, counting the vertices on the border itself).

3. Six disclinations remaining

We will now show that any border with winding number $W=0$ that does not intersect itself on a flat reference lattice is completable by applying a finite number of growth opera-

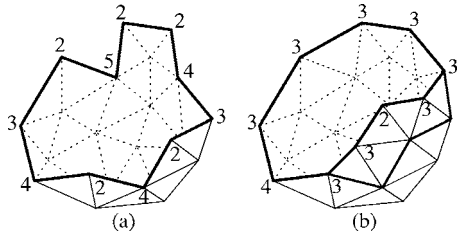

FIG. 13. Adding triangles to a $W=0$ border (a) to transform it into the self-complementary form 3^m23^n4 seen in (b).

tions to the border, resulting in a self-complementary border of the form 3^m43^n2, which can be glued onto a copy of itself to make a complete capsid.

First draw the border on a flat reference lattice. It is now clear that triangles can be added to the border to transform it to the required form. So any capsid with a nonintersecting border and $W \leqslant 0$ is completable.

This procedure is demonstrated in Figs. 13 and 14.

4. Late-stage completability

When $W>0$, there are more constraints. We can no longer add triangles freely since every row we add is smaller due to the enclosed disclinations. We will begin by considering the case of an incomplete capsid with 11 disclinations enclosed, leaving a deficit of one disclination needing to be placed.

a. One disclination remaining

In this case we can easily look at the reverse picture. If the border is completable then it is a path on a valid complete capsid and we can therefore look for a pseudocomplementary border to fill it. We can represent a triangular lattice with a single disclination as a flat triangular lattice with a 60° section cut out and the edges identified. If we therefore flatten our border onto a flat lattice, we expect the first and last points to be identified by this edge and therefore we can draw an equilateral triangle with the third point at the required location of the disclination. While the edges of the triangle need not be along a lattice direction, the third point is necessarily on the lattice. The border is completable if and only if this disclination is at an unoccupied point (outside of the original border). Note that because the border has a 60° rotation, this point is unique, regardless of the choice of starting and ending point. This process is demonstrated in Fig. 15.

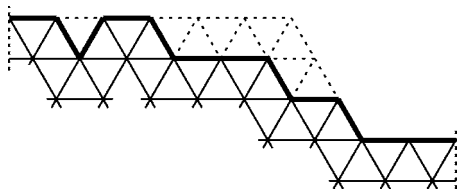

FIG. 14. An alternate point of view of the same procedure as illustrated in Fig. 13. We flatten the border onto a flat triangular reference lattice. The dashed lines on the left and right correspond to the place the border has been cut. That $W=0$ is evident because there is no net rotation after traversing the border. It is also clear that adding the dashed triangles results in the same 3^m23^n4 border as above.

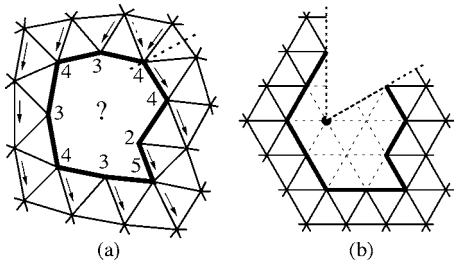

FIG. 15. A border with $W=5$. Parallel transporting a direction around the border yields a rotation of 60°. A disclination must therefore be located within this border. The dashed line shows where we plan to cut. (b) We see the same border flattened onto a reference lattice. The 60° rotation is now more clear. The dashed lines are part of an equilateral triangle and therefore show the required location of a disclination. Any choice of cut results in the same location, as long as the angle of the cut is chosen so that the triangle is equilateral.

b. Two disclinations remaining

Two disclinations ($W=4$) work in a very similar way to the single disclination discussed above, except we have a 120°-30°-30° isosceles triangle instead. This gives a single charge +2 disclination, but since we do not allow two disclinations at the same point, we must move them slightly. Figures 16 and 17 show the two possible situations and equivalent fillings with only single disclinations and the same border. If the center is on a lattice point, then the disclinations can each move in opposite directions to neighboring points and the same region of the plane will be cut out, up to a triangle at the apex, as shown in Fig. 16. If the center is in the center of a triangle rather than on a lattice point, we can place the two disclinations on adjacent lattice points around the triangle for the same effect, as shown in Fig. 17. The disclinations can be further separated in a similar fashion.

This breaks down if the +2 disclination is on a vertex on the border which has four or more triangles. In this case there is no way to separate the disclinations without one of them crossing the border.

c. Three disclinations remaining

The case of $W=3$ follows the same way, except now we find a +3 disclination on the midpoint of a line segment

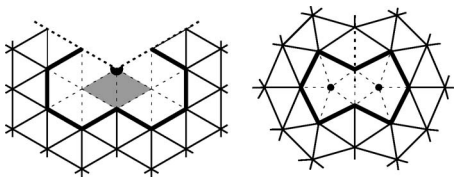

FIG. 16. Rearrangement of a +2 (120°) disclination located on a vertex into a pair of single disclinations with the same border. The two shaded triangles are removed.

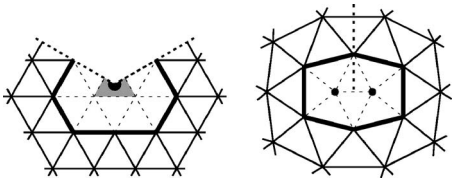

FIG. 17. Rearrangement of a +2 (120°) disclination located on a triangle into a pair of single disclinations with the same border. The shaded part of the triangle is removed.

joining the two identified points. This +3 disclination may be on a lattice point or on the edge of a triangle. Both can again be split similarly to the previous case, as seen in Figs. 18 and 19. As seen in the flattened pictures, the +3 disclination is always within the border, provided the flattened border does not intersect itself or the "cut line." Thus outside of these cases, the border is only incompletable if the +3 disclination cannot be split properly without any single disclinations crossing a border.

APPENDIX B: STERIC CONSIDERATIONS

Our triangular units are two-dimensional objects but they represent three-dimensional structures in space. Thus, we must explicitly ensure that two triangles can never be in positions, such that the proteins they represent would overlap in space. This appendix collects details concerning the implementation of steric constraints. First (Appendix B 1) we write the explicit form of the term in our Hamiltonian that prevents self-intersection; then (Appendix B 2) we discuss the way in which steric constraints tend to assist growth and to discourage the wrong steps that lead to failure.

1. Steric potential

The final term in Eq. (1) was a steric repulsion term: since our capsid units are two-dimensional triangles, some such term has to be added by hand, to account for the thickness of our three-dimensional proteins and disfavor unphysical configurations. The details of this term were deferred from Sec. II B to this appendix. The steric term should have the simplest possible form, in keeping with the toy-model spirit of our other terms.

In the steric term, the two kinds of degrees of freedom—topological and positional—clash in a sense. Two units that are nearby in space may be many steps apart on the bond network, and thus practically decoupled from each other.

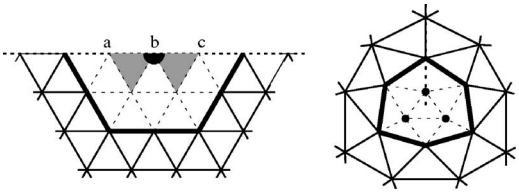

FIG. 18. Rearrangement of a +3 (180°) disclination located on a vertex into three single disclinations with the same border. The two shaded triangles are removed. Note that vertices *a*, *b*, and *c* all come together to form a single fivefold vertex.

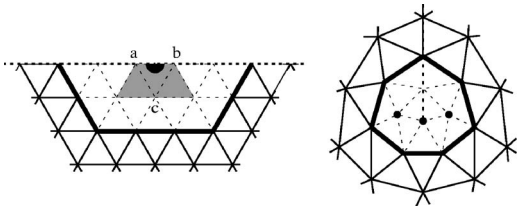

FIG. 19. Rearrangement of a +3 (180°) disclination located on an edge into three single disclinations with the same border. The three shaded triangles are removed and the vertices *a*, *b*, and *c* collapse to a single fivefold vertex.

(There is little interaction in the elastic energy, and furthermore, the ways they constrain the available discrete growth steps are independent.) Hence, $\mathcal{H}_{\text{steric}}$ must consist of topologically long-range, but positionally short-range, interactions.

We chose an implementation based on augmenting each triangle by another vertex over the face (on the interior side), thus forming a tetrahedron. We define a repulsion between the apex vertex of each tetrahedron and every (nonapex) vertex of every other triangle. Thus,

$$\mathcal{H}_{\text{steric}} = \sum_{I,j} V_{\text{steric}}(|\mathbf{r}_I^{\Delta} - \mathbf{r}_j|), \tag{B1}$$

where Σ_I is a sum over triangles and $\mathbf{r}_I^{\Delta}$ is an equal distance $\ell_{\text{steric}} \lesssim r_0$ inward from the three vertices of the triangle. Furthermore, we require $V_{\text{steric}}(r)=0$ if $r \geqslant \ell_{\text{steric}}$, which is the case for all pairs I,j in most capsids. This form allows the edges of unconnected triangles to be incident while maintaining $\mathcal{H}_{\text{steric}}=0$ so long as the triangles do not actually intersect.

We choose the simplest form, that is differentiable at $r=0$ and $r=\ell_{\text{steric}}$,

$$V_{\text{steric}}(r) = k_{\text{steric}}(\ell_{\text{steric}}^2 - r^2)^2, \quad r < \ell_{\text{steric}}. \tag{B2}$$

Choosing $\ell_{\text{steric}} \approx 0.65 r_0$ generally provides sufficient stericity while not interfering with the shape of non-self-intersecting capsids.

It is important to stress that this steric term should not affect most capsids. For nongrowing capsids, we generally turn it off to increase efficiency, since it always vanishes.

2. Steric growth heuristics

While the steric potential discussed in Appendix B 1 is useful to prevent capsids from relaxing to unphysical positions, it does not directly help the growth rules. Because growth rules are based entirely on rates k_A, k_I, and k_J derived from the local geometry around individual vertices, there is no way to directly determine whether a step will cause a steric hindrance. Because such growth steps are not likely to occur in nature, we implement a heuristic to detect such steps and remove them from the set of allowed growth steps by setting the rate to zero.

Before any accretion or insertion, we perform two tests. First we look at the steric potential $\mathcal{H}_{\text{steric}}$. If the accretion

causes $\mathcal{H}_{\text{steric}} \neq 0$, then the accretion fails. Next, if the accretion causes the centroid of one triangle to be within $\ell_{\text{steric}}/\sqrt{10}$ of the vertex of another triangle, then the accretion fails. This is necessary because the first test misses the case where two triangles are directly on top of one another. This case is less important while minimizing, because minimization would need to pass a large energy barrier, while growth steps can jump over it for free.

[1] S. O. Kim, H. H. Solak, M. P. Stoykovich, N. J. Ferrier, J. J. De Pablo, and P. F. Nealey, Nature (London) **424**, 411 (2003).
[2] J. Y. Cheng, A. M. Mayes, and C. A. Ross, Nat. Mater. **3**, 823 (2004).
[3] D. H. Gracias, J. Tien, T. L. Breen, C. Hsu, and G. M. Whitesides, Science **289**, 1170 (2000).
[4] G. M. Whitesides and B. Grzybowski, Science **295**, 2418 (2002).
[5] D. J. Kushner, Bacteriol. Rev. **33**, 302 (1969).
[6] R. N. Perham, Philos. Trans. R. Soc. London, Ser. B **272**, 123 (1975).
[7] M. F. Carlier, Adv. Biophys. **26**, 51 (1990).
[8] F. U. Hartl and J. Martin, Curr. Opin. Struct. Biol. **5**, 92 (1995).
[9] T. Ito, M. Bulger, M. J. Pazin, R. Kobayashi, and J. T. Kadonaga, Cell **90**, 145 (1997).
[10] N. Kimizuka and T. Nakashima, Langmuir **17**, 6759 (2001).
[11] J. N. Israelachvili, D. J. Mitchell, and B. W. Ninham, Biochim. Biophys. Acta **470**, 185 (1977).
[12] D. M. Salunke, D. L. D. Caspar, and R. L. Garcea, Cell **46**, 895 (1986).
[13] R. F. Bruinsma, W. M. Gelbart, D. Reguera, J. Rudnick, and R. Zandi, Phys. Rev. Lett. **90**, 248101 (2003).
[14] V. S. Reddy, H. A. Giesling, R. T. Morton, A. Kumar, C. B. Post, C. L. Brooks, and J. E. Johnson, Biophys. J. **74**, 546 (1998).
[15] It was noted early that capsids ought to be built from many identical copies of comparatively small proteins, in order to maximize the volume available for the genome, while minimizing the space on the genome needed to code them (Ref. [64]). However, point-group symmetries set an upper limit of 60 units, which can be joined equivalently to form a closed convex polyhedron (Refs. [16,64]); thus many proteins must be inequivalent by the symmetry.
[16] D. L. D. Caspar and A. Klug, Cold Spring Harbor Symp. Quant. Biol. **27**, 1 (1962).
[17] L. Pauling, Discuss. Faraday Soc. **13**, 170 (1953).
[18] R. Twarock, J. Theor. Biol. **226**, 477 (2004).
[19] R. Zandi, D. Reguera, R. F. Bruinsma, W. M. Gelbart, and J. Rudnick, Proc. Natl. Acad. Sci. U.S.A. **101**, 15556 (2004).
[20] J. Lidmar, L. Mirny, and D. R. Nelson, Phys. Rev. E **68**, 051910 (2003).
[21] B. Berger, P. W. Shor, L. T. Kellogg, and J. King, Proc. Natl. Acad. Sci. U.S.A. **91**, 7732 (1994).
[22] R. Schwartz, P. W. Shor, P. E. Prevelige, and B. Berger, Biophys. J. **75**, 2626 (1998).
[23] R. Schwartz, R. L. Garcia, and B. Berger, Virology **268**, 461 (2000).
[24] A. Zlotnick, J. Mol. Biol. **241**, 59 (1994).
[25] A. Zlotnick, J. Mol. Recognit. **18**, 479 (2005).
[26] T. Keef, A. Taormina, and R. Twarock, Phys. Biol. **2**, 175 (2005).
[27] B. K. Ganser, S. Li, V. Y. Klishko, J. T. Finch, and W. I. Sundquist, Science **283**, 80 (1999).
[28] V. M. Vogt and M. N. Simon, J. Virol. **73**, 7050 (1999).
[29] J. A. G. Briggs, M. N. Simon, I. Gross, H. G. Kräusslich, S. D. Fuller, V. M. Vogt, and M. C. Johnson, Nat. Struct. Mol. Biol. **11**, 672 (2004).
[30] J. A. G. Briggs, T. Wilk, R. Welker, H. G. Kräusslich, and S. D. Fuller, EMBO J. **22**, 1707 (2003).
[31] J. Lanman, T. T. Lam, M. R. Emmett, A. G. Marshall, M. Sakalian, and P. E. Prevelige, Nat. Struct. Mol. Biol. **11**, 676 (2004).
[32] J. A. G. Briggs, K. Grunewald, B. Glass, F. Forster, H.-G. Kräusslich, and S. D. Fuller, Structure (London) **14**, 15 (2006).
[33] J. Benjamin, B. K. Ganser-Pornillos, W. F. Tivol, W. I. Sundquist, and G. J. Jensen, J. Mol. Biol. **346**, 577 (2005).
[34] L. S. Ehrlich, T. B. Liu, S. Scarlata, B. Chu, and C. A. Carter, Biophys. J. **81**, 586 (2001).
[35] R. L. Kingston, N. H. Olson, and V. M. Vogt, J. Struct. Biol. **136**, 67 (2001).
[36] B. K. Ganser-Pornillos, U. K. von Schwedler, K. M. Stray, C. Aiken, and W. I. Sundquist, J. Virol. **78**, 2545 (2004).
[37] M. Ge and K. Sattler, Chem. Phys. Lett. **220**, 192 (1994).
[38] T. T. Nguyen, R. F. Bruinsma, and W. M. Gelbart, Phys. Rev. E **72**, 051923 (2005).
[39] T. T. Nguyen, R. F. Bruinsma, and W. M. Gelbart, Phys. Rev. Lett. **96**, 078102 (2006).
[40] D. Endres, M. Miyahara, P. Moisant, and A. Zlotnick, Protein Sci. **14**, 1518 (2005).
[41] A. Zlotnick, R. Aldrich, J. M. Johnson, P. Ceres, and M. J. Young, Virology **277**, 450 (2000).
[42] J. A. Speir, S. Munshi, G. Wang, T. S. Baker, and J. E. Johnson, Structure (London) **3**, 63 (1995).
[43] P. Forrer, C. Chang, D. Ott, A. Wlodawer, and A. Pluckthun, J. Mol. Biol. **344**, 179 (2004).
[44] Z. Xie and R. W. Hendrix, J. Mol. Biol. **253**, 74 (1995).
[45] U. K. von Schwedler, K. M. Stray, J. E. Garrus, and W. I. Sundquist, J. Virol. **77**, 5439 (2003).
[46] D. C. Rapaport, Phys. Rev. E **70**, 051905 (2004).
[47] D. Endres and A. Zlotnick, Biophys. J. **83**, 1217 (2002).
[48] A. Zlotnick, J. Chin. Inst. Eng. **315**, 269 (2003).
[49] H. S. Seung and D. R. Nelson, Phys. Rev. A **38**, 1005 (1988).
[50] S. Li, C. P. Hill, W. I. Sundquist, and J. T. Finch, Nature (London) **407**, 409 (2000).
[51] These are both consequences of the Euler characteristic for a genus zero surface, $\chi(g)=2-2g=2$. More generally, $V-E+F=\chi(g)$, and the total disclination charge must sum to $2\pi\chi(g)$. For more information, see Eric W. Weisstein, "Euler Characteristic." From MathWorld—A Wolfram Web Resource. http://mathworld.wolfram.com/EulerCharacteristic.html and references therein.

[52] Indeed, the CA protein in HIV consists of two separate domains, arranged in a wedge shape with the smaller *C*-terminal domain pointing towards the inside of the capsid and the larger *N*-terminal domain on the outside. See, for instance, the structures in Ref. [45]. RSV is similar [65].
[53] G. A. Vliegenthart and G. Gompper, Biophys. J. **91**, 834 (2006).
[54] I. L. Ivanovska, P. J. de Pablo, B. Ibarra, G. Sgalari, F. C. Mackintosh, J. L. Carrascosa, C. F. Schmidt, and G. J. Wuite, Proc. Natl. Acad. Sci. U.S.A. **101**, 7600 (2004).
[55] T. Maeda and S. Fujime, Macromolecules **18**, 2430 (1985).
[56] K. Zimmermann, H. Hagedorn, C. C. Heuck, M. Hinrichsen, and H. Ludwig, J. Biol. Chem. **261**, 1653 (1986).
[57] For a discussion of the geometric considerations in phage head assembly, see M. F. Moody, J. Mol. Biol. **293**, 401 (1999).
[58] A sevenfold vertex has a negative disclination charge; there must be a fivefold vertex next to it, with its positive disclination charge so the interior of the loop is neutral. A pair or "dipole" of positive and negative disclinations constitutes a *dislocation*. Its presence could have been concluded by the nonzero Burgers vector associated with that same loop; that is, the sum of the lattice displacements of each step, referenced to the ideal triangular lattice that can exist far away from this hole.
[59] M. Piatak, M. S. Saag, L. C. Yang, S. J. Clark, J. C. Kappes, K. C. Luk, B. H. Hahn, G. M. Shaw, and J. D. Lifson, Science **259**, 1749 (1993).
[60] D. M. Alamo and M. G. Mateu, J. Mol. Biol. **345**, 893 (2005).
[61] G. B. Mortuza, L. F. Haire, A. Stevens, S. J. Smerdon, J. P. Stoye, and I. A. Taylor, Nature (London) **431**, 481 (2004).
[62] B. Shraiman, Biophys. J. **72**, 953 (1997).
[63] N. Socci and B. Shraiman (private communication).
[64] F. H. C. Crick and J. D. Watson, Nature (London) **177**, 473 (1956).
[65] N. Nandhagopal, A. A. Simpson, M. C. Johnson, A. B. Francisco, G. W. Schatz, M. G. Rossmann, and V. M. Vogt, J. Mol. Biol. **335**, 275 (2004).